



Phosphorous doped carbon nitride nanobelts for photodegradation of emerging contaminants and hydrogen evolution



Shuaijun Wang^{a,b}, Fengting He^a, Xiaoli Zhao^b, Jinqiang Zhang^b, Zhimin Ao^c, Hong Wu^b, Yu Yin^b, Lei Shi^b, Xinyuan Xu^b, Chaocheng Zhao^{a,*}, Shaobin Wang^d, Hongqi Sun^{b,*}

^a State Key Laboratory of Petroleum Pollution Control, China University of Petroleum (East China), Qingdao, 266580, PR China

^b School of Engineering, Edith Cowan University, 270 Joondalup Drive, Joondalup, WA, 6027, Australia

^c Guangzhou Key Laboratory of Environmental Catalysis and Pollution Control, Institute of Environmental Health and Pollution Control, School of Environmental Science and Engineering, Guangdong University of Technology, Guangzhou, 51006, China

^d School of Chemical Engineering, The University of Adelaide, Adelaide, SA, 5005, Australia

ARTICLE INFO

Keywords:
Photocatalysis
Carbon nitride
P-doping
HBA degradation
Hydrogen production

ABSTRACT

Photocatalysis has demonstrated great potentials for both environmental remediation and green energy production. In this study, a simple solvothermal template-free approach was employed for the first time to synthesize phosphorous doped carbon nitride nanobelt (P–CN–NB). Advanced characterizations, for instance, ¹³C NMR, ³¹P NMR, and XPS results indicated that P was substitutionally doped at the corner-carbon of the carbon nitride frameworks. The introduction of P dopants inhibited the polymerization between NH₂ groups within P–CN–NB, enabling the decrease in nanobelt width for the exposure of more active sites. Therefore, the optimized P–CN–NB–2 (derived from 0.2 mM H₃PO₄) rendered enhanced p-hydroxybenzoic acid (HBA) degradation nearly 66-fold higher than bulk g-C₃N₄, among the most efficient g-C₃N₄-based photocatalysts as reported. In addition, the P–CN–NB–1 (derived from 0.02 mM H₃PO₄) exhibited about 2 times higher H₂ evolution rate than CN–NB. Density functional theory (DFT) calculations were also conducted to provide insights into the mechanism.

1. Introduction

Persistent organic pollutants (POPs) in waste water have become a worldwide concern because of the detrimental effect on the human's sustainable development [1]. P-hydroxybenzoic acid (HBA) as an emerging pollutant can hardly be decomposed by a conventional method, and remains a great challenge for a green and effective remediation technology [2]. Solar-driven photocatalysis is attracting considerable attention because it has been proven to be an emerging green and sustainable technology to address the global environmental and energy issues in the future [3–6]. Apart from the solar light harvesting, the selection of a suitable semiconductor is also the critical point in the photocatalysis process. Inorganic semiconductors, such as TiO₂ [7–9], ZnO [10–12], WO₃ [13,14], a-Fe₂O₃ [15], Cu₂O [16] and many others, have been extensively studied as the photocatalysts or photoelectrocatalysts. However, their efficiencies, environmental-friendliness, and stability are not entirely satisfactory for practical applications [17,18]. Therefore, the design of robust, highly efficient, and cost-effective semiconductors is still challenging. Recently, a metal-free

polymeric photocatalyst, graphitic carbon nitride (g-C₃N₄), was reported and employed in versatile photocatalysis processes owing to its tunable electronic band structure, environmental benignity, excellent physicochemical stability, and cost-effectiveness [19–21]. However, some drawbacks including fast recombination of electron-hole pairs, poor electrical conductivity, high synthesis temperature, and the degradation of responsivity above 460 nm, etc., dramatically hindered its practical applications [22,23].

To address these problems, great efforts such as designing a heterostructure [24–26], heteroatom doping [27], and tailoring morphologies [28,29] have been devoted to optimizing the photocatalytic performance of g-C₃N₄. In terms of the morphological control, hard template [30,31], soft template [32], and supramolecular copolymerization [33,34] are the conventional used approaches. However, the hard template methods usually require toxic chemicals, for instance, HF to remove the template, making the process highly hazardous. For the soft template and supramolecular copolymerization methods, the synthesized morphologies are uncontrollable due to a large amount of NH₃ being released, which will also pose a threat to the morphology.

* Corresponding authors.

E-mail addresses: zhaochch@upc.edu.cn (C. Zhao), h.sun@ecu.edu.au (H. Sun).

Template-free approach at low temperatures (180–200 °C) is of great interest owing to its easy-handling, good controllability, and green features [35,36]. In addition, this method has been reported and employed in the synthesis of carbon nitride [37,38]. For example, Cui et al. [39] successfully fabricated carbon nitride with nanobelt structures via the template-free method, and the nanobelt content accounts for more than 90% of the gained samples. The prepared samples exhibited dramatically enhanced visible light absorption capability, a larger surface area, and much higher oxidation activity. More interestingly, this method combined the solution assembly, molecular engineering, crystallization, and covalent cross-linking chemistry in one pot, and thus the resulting sample became very efficient and attractive. The band-gap energy of the carbon nitride nanobelt (CN–NB) was much lower than that of pristine $\text{g-C}_3\text{N}_4$, which could be the result of the morphological change of the sample [40]. However, during the synthesis process of CN–NB, oxygen (O) and chlorine (Cl) were simultaneously introduced into the system, and the roles of O and Cl remains unclear.

Besides the morphology control approach, heteroatom doping is another promising and effective strategy because it can simultaneously regulate the electronic band edges, the visible light absorption ability, and the conductivity [41–43]. Recently, it was reported that phosphorus (P) monomer [44] or P-doped carbon nitride [45,46] exhibited enhanced performances for H_2 evolution or CO_2 reduction. For example, Ran et al. [45] demonstrated that P doped porous carbon nitride nanosheet achieved a hydrogen AQE of 3.56% at 420 nm, which was the highest value among metal-free-carbon nitride catalysts at the time. Later, P doped carbon nitride tubes were designed by a combined hydrothermal process with post annealing approach, with a 5.68% AQE at 420 nm achieved [46]. Nevertheless, these methods need two or more steps, resulting in the complexity of the fabrication process. In addition, the morphology of the grain size was large, which is unfavorable to the photocatalysis process. Besides, the potential of the valence band (VB) was decreased, which significantly limited the oxidation activity. Therefore, designing novel and simple synthesis process for producing P-doped carbon nitride with a smaller grain size and high oxidation ability still remains a great challenge.

In this work, we developed a facile template-free solvothermal approach to prepare P-doped carbon nitride nanobelt (P–CN–NB). During this process, the P doping, band-gap engineering, and morphology control can be simultaneously achieved in one pot fashion. The chemical compositions and the structures of the fabricated samples were studied by ^{13}C NMR, ^{31}P NMR, and XPS, and the results indicated that P was substitutionally doped into the position of the corner-carbon within the carbon nitride framework. The optimized photocatalyst was highly efficient for photocatalytic HBA degradation (66-fold enhancement degradation rate than bulk $\text{g-C}_3\text{N}_4$). Experimental results, along with density functional theory (DFT) calculations, indicated that the enhanced photocatalytic degradation efficiency of P–CN–NB is derived from its specific electronic structure and the unique asymmetric LUMO orbital configuration by significantly promoting the electron-hole separation and kinetic reactions.

2. Experimental section

2.1. Preparation of P–CN–NB

The synthesis process for P–CN–NB is exhibited in **Scheme 1**. P–CN–NB was synthesized via a one-pot solvothermal approach. In detail, melamine (8 mM), cyanuric chloride (16 mM), and different amounts of H_3PO_4 (0.02, 0.2, 0.4, and 0.8 mM, respectively) were dissolved in a 100 mL autoclave (with 60% of acetonitrile). The solution was dramatically stirred for 24 h. Then, the homogeneous suspension was sealed and placed into an oven at 180 °C for 24 h. After cooling to the room temperature and washing with acetonitrile, ethanol, and distilled water for three times, the P doped carbon nitride composites were obtained. According to the dosage of H_3PO_4 (0.02, 0.2, 0.4, and

0.8 mM), the prepared photocatalysts were denoted as P–CN–NB-1, P–CN–NB-2, P–CN–NB-3, and P–CN–NB-4, respectively. CN–NB sample was synthesized via the same approach without the addition of H_3PO_4 . The bulk $\text{g-C}_3\text{N}_4$ was prepared via the thermal polymerization method as can be seen elsewhere [47].

The working electrodes were prepared via the simple dipping method. Before making the electrodes, the 1.5 cm × 1.0 cm FTO glasses were washed using acetone, ethanol, and distilled water under sonication. The working electrodes were prepared as below: 5 mg catalyst, 20 μL 117 Nafion solution, and 500 μL ultrapure water were mixed under sonication, and 20 μL of the resulting slurry was loaded onto the 1.0 cm × 1.0 cm FTO. The working electrodes were dried in air overnight.

2.2. Characterization

The transmission electron microscopy (TEM) was performed on a JEOL 2100 TEM instrument (120 kV). The high angle annular dark field scanning transmission electron microscopy image (HAADF-STEM) mapping was acquired on FEI TITAN G2 (200 kV). XRD patterns were obtained on a Holland X'Pert Pro diffractometer. FT-IR spectra of the samples were recorded on a Nicolet Nexus 670 spectrometer (400 to 4000 cm^{-1}). The nitrogen adsorption-desorption isotherms were evaluated on a Micromeritics sorption analyzer (ASAP 2010). X-ray photoelectron spectroscopy (XPS) studies were conducted using an ESCALAB 250xi spectrometer. The UV-vis diffuse reflectance and photoluminescence (PL) spectra were collected on a TU-1901 spectrometer and a Hitachi F-4500 Fluorescence spectrophotometer, respectively. Electron paramagnetic resonance (EPR) spectroscopy was applied for the catalysts (Bruker A200). NMR was carried out on a Bruker ADVANCEIII 500 MHz equipment.

2.3. Photoelectrochemical and photocatalytic activity

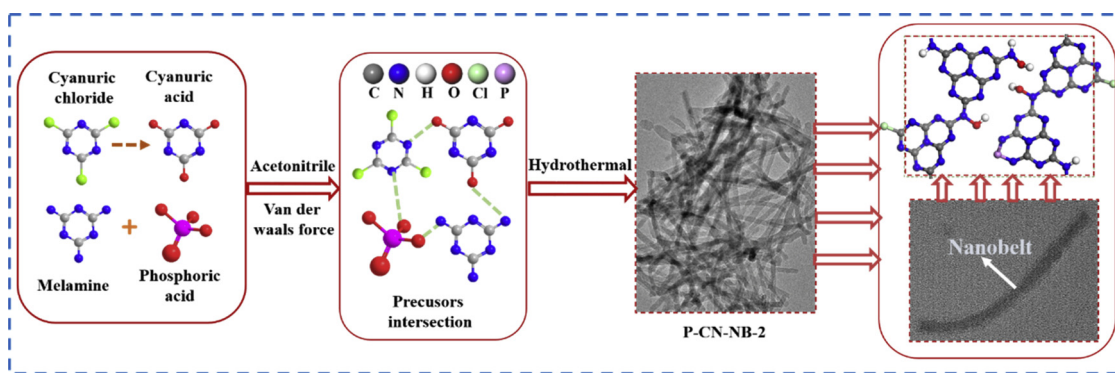
The photocurrents and electrochemical impedance spectra (EIS) were acquired on a Zennium electrochemical system (Zahner, Germany) in a three-electrode cell, with the catalysts/FTO as the working electrode, a saturated Ag/AgCl electrode as the reference electrode, and a platinum plate as the counter electrode.

For each photodegradation experiment, 25 mg of the catalyst was added into 50 mL of HBA aqueous solution (1 ppm). A 300 W Xe lamp (Newport, output intensity: 1 sun) with a 420 nm cut off filter was selected as the light source. Prior to the irradiations, the HBA suspensions were stirred in the dark for 30 min to reach the adsorption-desorption equilibrium. After the xenon lamp was turned on, 2.0 mL suspensions were sampled every 20 min, and the concentration of HBA was analyzed using a high-performance liquid chromatography (Shimadzu HPLC) equipped with a UV detector at the detection wavelengths of 276 nm and a C18 column (2.7 μL , 100 × 2.1 mm). Total organic carbon (TOC) analyzer was provided by Shimadzu Corporation.

The photocatalytic efficiencies were also evaluated by monitoring the hydrogen evolution, which was conducted in a closed on-line photocatalytic system. Briefly, 25 mg of the catalyst powder was added to an aqueous solution (25 mL) containing 2.5 mL of TEOA and 0.4 mL of 3.0 wt% $\text{H}_2\text{PtCl}_6\text{(H}_2\text{O)}_6$ and sonicated for 30 min. Prior to the visible light irradiations, the reactor was evacuated by a vacuum pump to remove air. The solution was then irradiated by a 300 W Xe lamp (perfectLight) with a cut-off filter, under magnetic stirring, to produce H_2 . The evolved hydrogen was analyzed by an online gas chromatograph (GC7920, Techcomp, TCD detector, carrier gas: N_2 , 5A molecular sieve column).

2.4. Density-functional-theory (DFT) calculations

The CASTEP software package [48] was used for DFT calculations in this work. A plane wave basis set was adopted, together with the



Scheme 1. Schematic drawing of the formation process of P-CN-NB.

generalized gradient approximation (GGA) and Perdew-Burke-Ernzerhof (PBE) functional [49]. The Brillouin zone was sampled with $3 \times 3 \times 4$ k-point, and the cut off energy was set to 340 eV.

As the starting point, the pristine $\text{g-C}_3\text{N}_4$ sheet without doping was built as a benchmark. A series of models along the condensation path, from an isolated melon molecule of 22 atoms, then polymeric melon sheet consisting 72 atoms in a unit cell, and finally to the hypothetically, fully condensed, infinite $\text{g-C}_3\text{N}_4$ sheet, were constructed, seen in Fig. S1 in the Supplementary Data. For all the aforementioned models, the separation between different layers was set to 15 Å, so that the interaction between layers can be negligible. Because of the consistency with experimental results, this polymeric melon sheet model has been generally accepted and widely applied in recent studies [50–52]. The lattice parameters of the polymeric melon are 16.7×12.4 Å [53]. During the DFT calculations, we assigned different sites for the P, O and Cl atoms with the XPS experimentally derived atomic proportion, i.e., C: N: Cl: O: P = 35: 52: 3: 10: 1, in order to determine the site occupancy of the Cl, O and P atoms within the samples. In the calculations, we first identified those models after geometry optimization which yielded agreement with experimental site occupancy indicator. Then, amongst these models, we selected the one which has the lowest free energy in a unit cell.

3. Results and discussion

Fig. 1 exhibits the HRTEM images of the prepared carbon nitride samples. The pristine $\text{g-C}_3\text{N}_4$ exhibited a bulk structure, while CN–NB showed a nanobelt structure, and the width was about 100 nm. For P–CN–NB–2, the nanobelt structure was also obtained, while the width was reduced to approximately 18 nm. It was seen that the incorporation of P did not change the general morphology but made the hierarchical nanobelt narrower. The decrease in the width was because the P dopants might inhibit the polymerization between NH_2 groups in the heptazine units. HAADF-STEM and EDX elemental mapping images of P–CN–NB–2 indicated that the P was uniformly incorporated into the carbon nitride framework.

XRD patterns of the $\text{g-C}_3\text{N}_4$, CN–NB, and P–CN–NB samples (Fig. 2a) all exhibited a typical reflection at 27.3° , which is associated with the (002) interlayer of $\text{g-C}_3\text{N}_4$. However, the peaks of CN–NB and P–CN–NB samples are much broader and weaker than that of $\text{g-C}_3\text{N}_4$ synthesized at a high temperature. This is probably because of the less ordered stacking of tri-s-triazine units [27]. In addition, the peaks at 13° cannot be seen on the samples synthesized in solution, suggesting the existence of some disordered crystal structure [54,55]. Some new peaks were observed on the samples of P–CN–NB, which may be due to the presence of melem derivatives [56,57]. It was also found that when the adding amount of H_3PO_4 was 0.8 mM, the formation of carbon nitride was retarded, which can be confirmed by the results of XRD and FT-IR (Fig. S2 a–b). The corresponding photocatalytic activity for HBA degradation was deficient (Fig. S2 c). Therefore, the adding dosage of

H_3PO_4 should be not over 0.8 mM.

In the FT-IR spectra (Fig. 2b), all the samples exhibited the absorption bands at 812 cm^{-1} and between 3000 and 3600 cm^{-1} , which are from the breathing mode of the triazine units, and the N–H stretching vibration bonds, respectively [58]. The absorption band of $\text{g-C}_3\text{N}_4$ and CN–NB at 1200 – 1700 cm^{-1} originated from CN heterocycles [59], while P–CN–NB samples showed two broad groups at 1596 and 1442 cm^{-1} , coinciding with those of melem [57]. In addition, the obvious –OH and $\text{C}=\text{O}$ bands were observed at 3400 and 1750 cm^{-1} on the CN–NB and P–CN–NB, respectively. No vibration modes for P-related groups of P–CN–NB were detected, probably because of the low percentage or signal over-lapping.

The nitrogen sorption isotherms of the $\text{g-C}_3\text{N}_4$, CN–NB, and P–CN–NB samples (Figs. 2c and S3a) exhibited type IV isotherms with H3 hysteresis, reflecting the existence of mesopores. The desorption pore distribution (Figs. 2d and S3b) indicated that all the samples possess a bimodal distribution, and the corresponding parameters are listed in Table S1. The specific surface area of P–CN–NB is $33.7 \text{ m}^2 \text{ g}^{-1}$, about 5 and 2 times larger than that of $\text{g-C}_3\text{N}_4$ and CN–NB, respectively. The enlarged surface areas of P–CN–NB may be due to the decreased size of nanobelt, which could provide more surface active sites. The unique nanobelt structure and the P heteroatoms are expected to not only modulate the electronic band structure, but increase the electron-hole separation efficiency of the CN–NB.

Further elemental compositions and chemical states of $\text{g-C}_3\text{N}_4$, CN–NB, and P–CN–NB–2 were analyzed by XPS, and the atomic percentage of $\text{g-C}_3\text{N}_4$, CN–NB, and P–CN–NB–2 are shown in Table S2. The XPS C 1s spectra (Fig. 3a) at 284.8, 286.6, and 288.5 eV were due to sp^2 graphitic carbon (C–C bonding), adventitious carbon (C=C), and sp^2 -bonded carbon in the s-triazine units (N–C = N), respectively [60]. For the N 1s spectra (Fig. 3b), the peaks at 398.8, 399.9, and 400.7 eV correspond to the C=N, N–(C)₃, and C–NH₂, respectively [61]. The O 1s (Fig. S4a) of CN–NB and P–CN–NB–2 possess two peaks, with the binding energy at 531.7 eV (–OH) and 533.4 eV (C=O) [54]. For the $\text{g-C}_3\text{N}_4$ catalyst, only surface hydroxyl groups were observed at 531.8 eV, suggesting that C=O cannot be formed on $\text{g-C}_3\text{N}_4$. The Cl 2p spectra (Fig. S4b) of CN–NB show two main peaks at approximately 200.7 eV for Cl 2p_{1/2} and 197.5 eV for Cl 2p_{3/2}. The first two peaks at 202.2 and 200.6 eV can be ascribed to C–Cl covalent bonds, and the second fitted peaks at 198.8 and 197.2 eV are attributed to Cl ionic bonds [54,62]. P–CN–NB showed a very low intensity in the first peak and a much strong intensity in the second peak, suggesting that the incorporation of P promotes the break of C–Cl bonds. The signal of P 2p (Fig. 3c) is located at approximately 133.6 eV, which is in accordance with P–N coordination, suggesting that P probably replaces C in the carbon nitride framework [46]. Solid NMR ¹³C (Fig. 3d) was further performed to unveil the structures of the $\text{g-C}_3\text{N}_4$, CN–NB, and P–CN–NB. All the samples exhibited two obvious signals at 156.4 and 164.5 ppm assigned to the C(1) atoms ($\text{C}_{3\text{N}}$) and C(2) atoms ($\text{C}_{2\text{N}-\text{NH}_2}$) in the melem, respectively. A new signal at 151.8 ppm can be observed

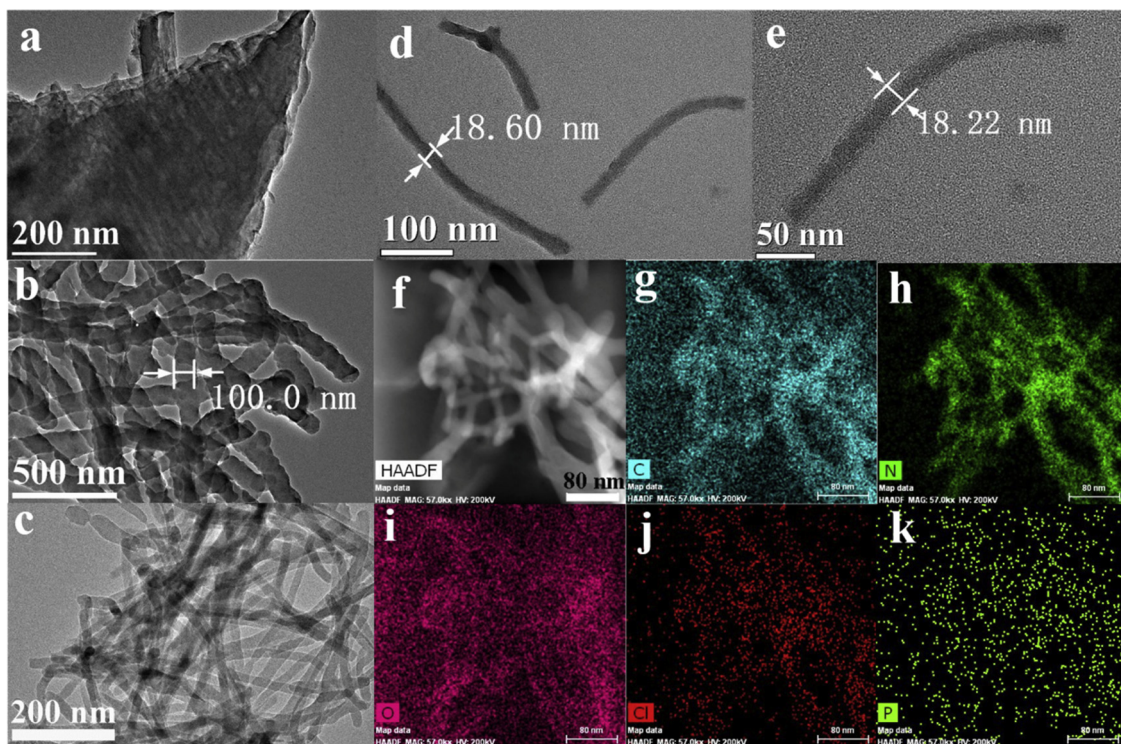


Fig. 1. TEM images of (a) g-C₃N₄, (b) CN-NB, (c)-(e) P-CN-NB-2, and (f)-(k) HAADF-STEM image of P-CN-NB-2 and the EDX elemental mapping analysis.

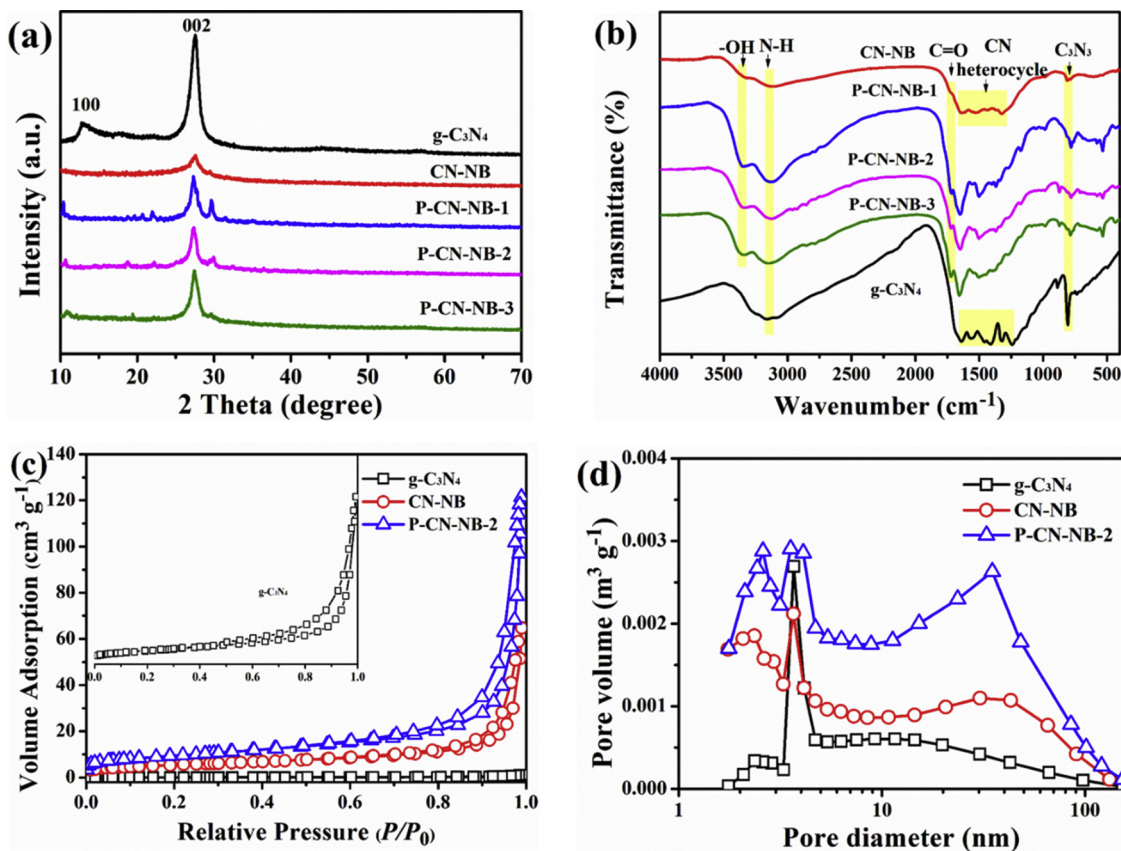


Fig. 2. (a) XRD patterns, (b) FT-IR spectra, (c) nitrogen sorption isotherms, and (d) pore size distribution of the synthesized catalysts.

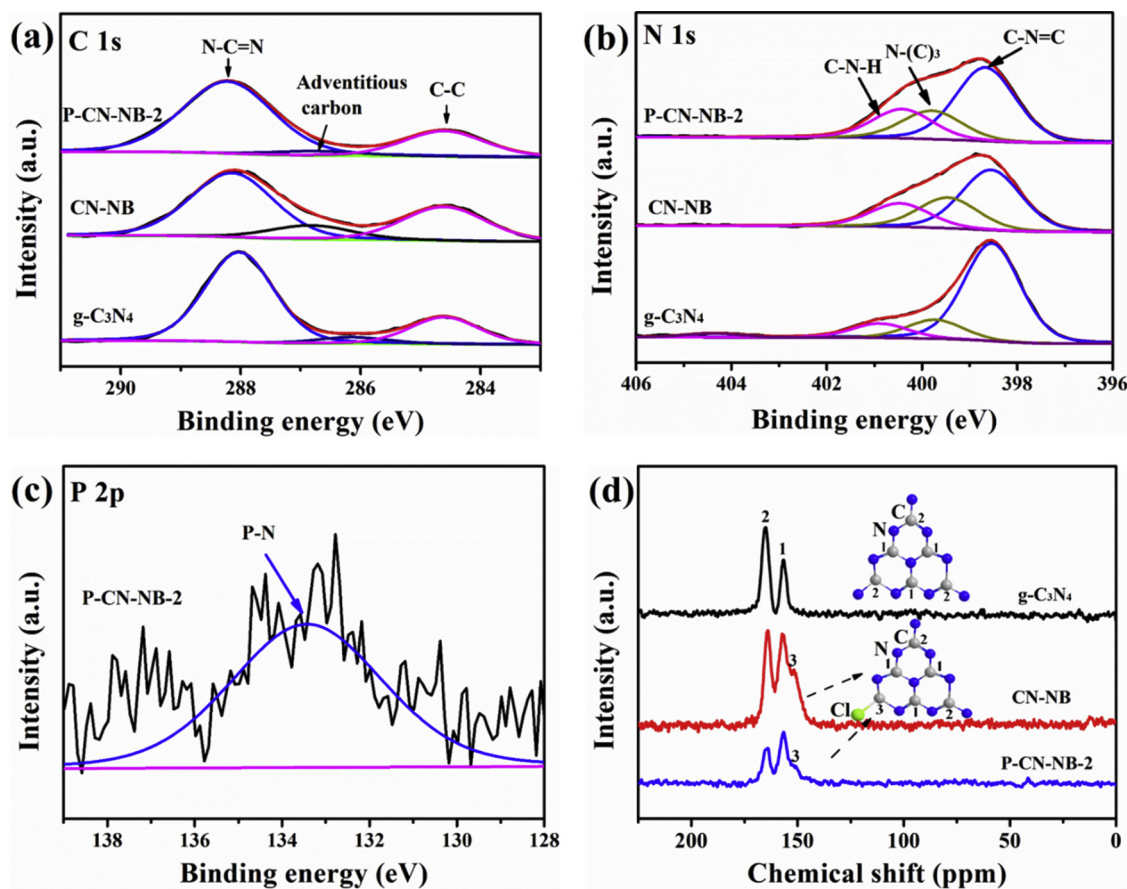


Fig. 3. XPS spectra of (a) C 1s, (b) N 1s, (c) P 2p, and (d) ^{13}C NMR spectra of the prepared samples.

for CN–NB and P-CN-NB-2, which can be attributed to the C(3) atoms (C_{Cl}). It should be noted that no P–C peak was observed on the P–C–N–NB, suggesting P substitutes C instead of N forming P–N bond, which agrees well with the results of XPS P 2p results. For further confirmation, solid-state ^{31}P was carried out. The NMR results of P-CN-NB-2 (Fig. S5) on the ^{31}P show two peaks at -6.65 and -7.95 ppm (the signals with * was due to the partial rotor between the sample and magnetic field of equipment), confirming that P was introduced in the framework with two different positions (1, the corner carbon, 2, the bay carbon) [63]. Our calculation results indicated that the substitution of P of corner carbon was with a reasonable band-gap energy and relatively low total energy (not shown) and that the replacement of P of bay carbon resulted in the carbon nitride framework distorted severely. Therefore, the substitution of corner carbon by P is preferred in P-CN-NB-2 system.

The UV–vis DRS of the g-C₃N₄, CN–NB, and P–CN–NB samples are exhibited in Fig. 4a. In comparison to g-C₃N₄ and CN–NB, the incorporation of P improved the visible light absorption ability. In addition, the band-gap energies of the g-C₃N₄, CN–NB, and P-CN-NB-2 samples (Fig. 4b) were determined to be 2.73, 2.24, and 2.19 eV, respectively. It can be seen that the band-gap of CN–NB was much narrower than the g-C₃N₄ prepared at a high temperature (2.6 ~ 2.8 eV), which can be attributed to the introduction of Cl and O element in the CN–NB frameworks. The VB position was further confirmed by the XPS technique. The VB edge of g-C₃N₄, CN–NB, and P-CN-NB-2 samples are 1.81, 2.24, and 2.19 eV, respectively. The estimated conduction band (CB) positions are then -0.92, -0.15, and -0.04 V for g-C₃N₄, CN–NB, and P-CN-NB-2, respectively. The band structure information of g-C₃N₄, CN–NB, and P-CN-NB-2 are exhibited in Fig. 4d and Table S3. The lowering of the VB indicates that P-CN-NB-2 possesses a stronger oxidation and a lower reduction ability theoretically.

For a deeper insight into the mechanism on the narrower band-gap taking place on the P-CN-NB-2 sample, DFT calculations for the band structure and density of states (DOS) were performed. The calculated band-gap of pristine g-C₃N₄ was 2.52 eV (Fig. 5b), in agreement with the results in the reported references [53,64], and also agrees with our experimental results on the pristine g-C₃N₄. By using hybrid functional the bandgap accuracy may be further improved, but which is computationally unaffordable in systems with large number of atoms [40]. Here we more concern on the band structure change trend after doping of different elements, so GGA-PBE is used in all the calculations. To demonstrate different contributions towards the total DOS, partial DOS (PDOS), with respect to contributions from orbitals of different elements (Fig. S6c), as well as to those from different bands (Fig. S6d), were presented, respectively. Within the range of -2 to 0 eV, nitrogen orbitals contribute towards VB predominantly, about 97%. In contrast, for the CB carbon orbitals have a higher contribution of ~ 55%. In particular, at a lower portion close to the CB edge, the proportion of C orbital contribution is more significant. When considering the contributions from different bands, the 2p contributions (combined from both C and N) to both VB and CB are predominant within the range energy range being studied. Close to the VB edge the 2s band orbitals only contribute ~ 10% to the total VB-DOS. Almost all the orbitals in the CB are provided by the 2p band from both C and N orbitals, while the 2s orbitals' contribution to CB is negligible. The results are consistent with those in previous studies [50,65].

To clarify the roles played by different elements in modifying the band structure, we first calculated the CN–NB, with the results given in Fig. 5. Compared to g-C₃N₄, similar contribution proportion C/N orbitals was observed on CN–NB. However, the CB edges of both C and N contributions were lowered, with the former being more significant. The contribution to CB from the orbitals of newly added elements, e.g.,

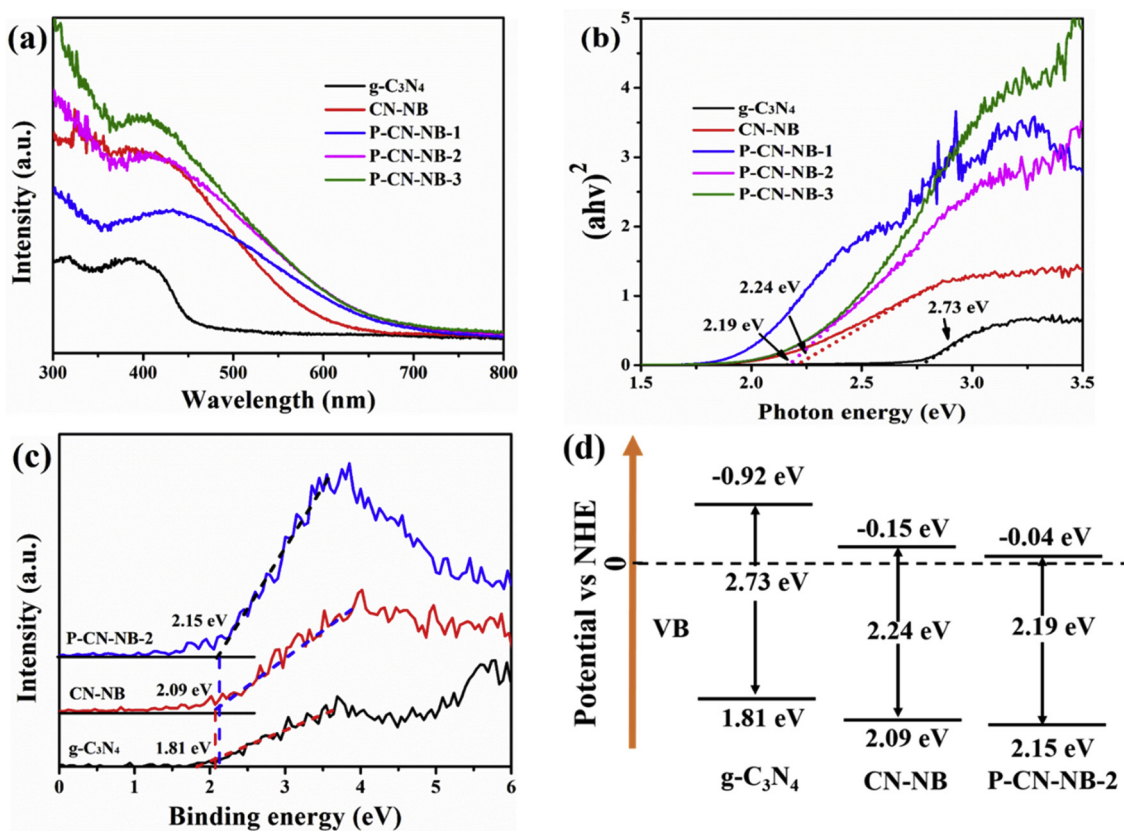


Fig. 4. (a) UV-vis diffuse reflection spectra, (b) the band-gap determination plots, (c) XPS valance band spectra, and (d) schematic band-gap structure of the prepared samples.

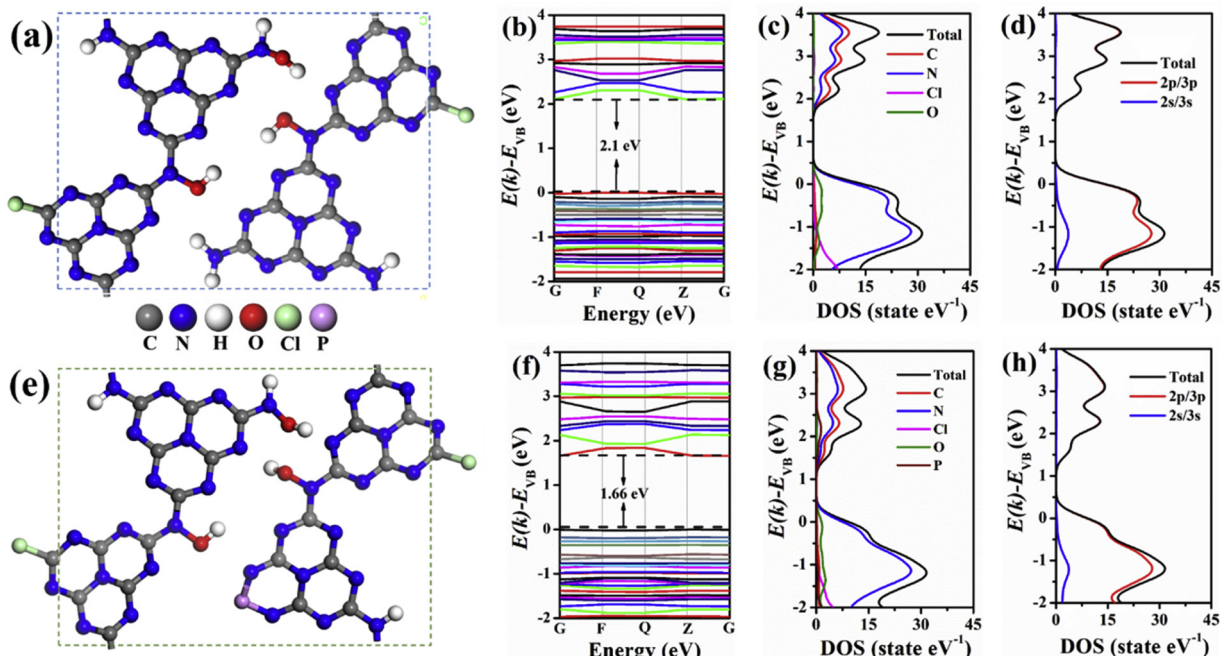


Fig. 5. DFT calculation results. (a) Optimized unit cell of CN-NB polymeric melon sheet used in the DFT calculations, (b) CN-NB band structure, (c) PDOS of CN-NB, decomposed with respect to contributions from different elements, (d) PDOS of CN-NB, decomposed with respect to contributions from orbitals within 2s/3s and 2p/3p bands, respectively, (e) optimized unit cell of P-CN-NB-2, (f) P-CN-NB-2 band structure, (g) PDOS of P-CN-NB-2, decomposed with respect to contributions from orbitals of diverse elements, and (h) PDOS of P-CN-NB-2, decomposed with respect to contributions from orbitals within 2s/3s and 2p/3p bands, respectively.

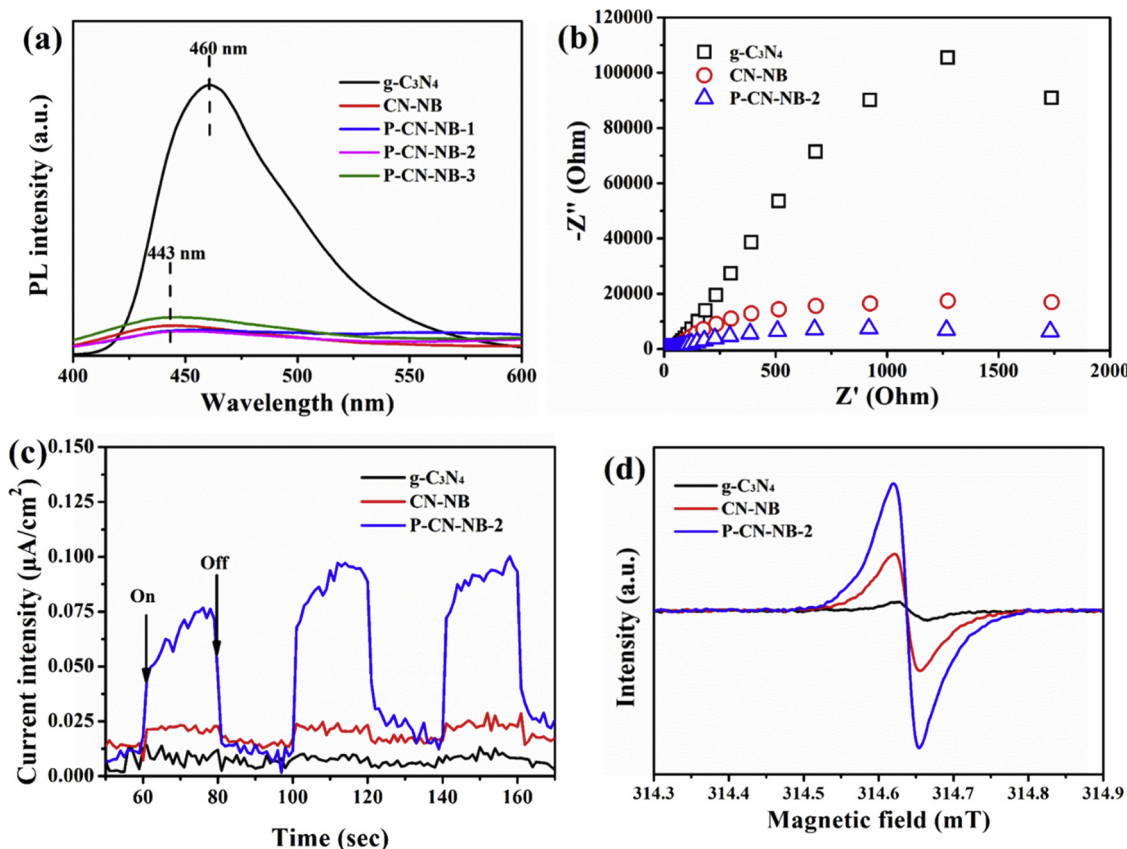


Fig. 6. (a) Photoluminescence spectra, (b) EIS, (c) photocurrent, and (d) ESR signals of the synthesized catalysts.

Cl and O, is negligibly small. N and O contributions to the VB starts immediately below the VB edge, while Cl and O contributions begin at a lower area < -1 eV. The optimized crystal structure of P-CN-NB from DFT calculation is shown in Fig. 5e. Both C and N orbital contributions are further lowered above the CB edge, with a significant portion located below 2 eV, resulting in a further narrowing of the band-gap (Fig. 5f). Interestingly, P orbitals also have a no-negligible contribution to the CB. A portion of the P contribution was found to be also located below 2 eV, which helped to push the narrowing of the band-gap (Fig. 5g). In terms of band contributions, similar to the situation on the pristine g-C₃N₄ and CN-NB, 2p bands from C, N, and 3p band from P are the predominant sources (Fig. 5h) which push the CB band edge downwards. From the DFT calculations, incorporating O and Cl resulted in the band-gap being reduced from 2.52 eV of pristine g to 2.10 eV on CN-NB (Fig. 5b), and the substitution of one C atom by a P atom resulted in a further decrease in the band-gap energy from 2.1 to 1.66 eV in P-CN-NB (Fig. 5f). The trend is consistent with the increasing absorption tail of the CN-NB and P-CN-NB (Fig. 4a).

In addition to the narrowed electronic band-gap structure, the P doping was expected to influence the process of charge transfer, which can be explored by PL, EIS, and photocurrent response. The carbon nitride prepared at a low temperature exhibited a dramatically weakened PL intensity than that of pristine g-C₃N₄ (Fig. 6a). The strong emission peak centered at 460 nm of g-C₃N₄ was because of the band-to-band recombination electron-hole pairs. Besides, CN-NB exhibited obvious blue-shift of PL maximum, which can be assigned to the disordered stacking in the layers. The incorporation of P showed a slight lower emission peak than that of CN-NB, but no shift of position was observed. In general, a large arc radius in the EIS indicates a higher resistance value, corresponding to the inefficient separation of photo-induced electrons and holes. Although the g-C₃N₄, CN-NB, and P-CN-NB-2 exhibited similar Nyquist plots (Fig. 6b), CN-NB and P-CN-NB-2 samples had a significantly smaller diameter, suggesting that CN-NB

and P-CN-NB-2 possess more efficient charge separation. Moreover, after the doping of the P element, the P-CN-NB-2 exhibited a much higher photocurrent intensity than that of g-C₃N₄ and CN-NB under solar light irritations. Furthermore, EPR measurement shows that the tensor parameter (g) of g-C₃N₄, CN-NB, and P-CN-NB-2 are 1.9995 (Fig. 6d). Usually, the stronger intensity of EPR signals will induce more unpaired electrons and result in a better electronic band structure. Therefore, P-CN-NB-2 possessed many unpaired electrons and a better electronic band structure than that of g-C₃N₄ and CN-NB.

Fig. 7a shows the photocatalytic activities toward HBA degradation on the prepared samples. With the visible light irradiations, the HBA degradation efficiency of g-C₃N₄ was very low, and CN-NB showed 33.1% efficiency toward HBA degradation with 120 min reaction. Notably, the optimized P-CN-NB-2 exhibited 77.3% HBA removal. The enhanced photocatalytic activity may be owing to the narrowed band-gap enabling the improved light absorption ability, the more efficient electron-hole separation, and the downward of the VB. In addition, the apparent rate constant (*k*) value (Fig. 7b and c) toward HBA degradation of P-CN-NB-2 was higher, about 2.8 and 66 times than that of CN-NB and g-C₃N₄, respectively. To the best of our knowledge, the enhanced degradation performance was higher than most reported g-C₃N₄-based composites in the degradation of refractory pollutants (Table S4). This result shows that the incorporation of P improved the photocatalytic activity of carbon nitride significantly. In addition, the mineralization ability towards HBA of P-CN-NB-2 was further evaluated by the TOC analysis. As shown in Fig. S7, after 120 min reaction under visible light irradiations, a 31.5% removal efficiency was achieved by the P-CN-NB-2, which was much higher than g-C₃N₄. This results indicated that P-CN-NB-2 possesses a strong oxidation ability that can achieve efficient TOC removal by mineralization.

The HBA photodegradation stability of the P-CN-NB-2 (Fig. 7d) was tested by repeated use of the catalyst for several times. After four successive runs, the photocatalytic activity of the P-CN-NB-2 catalyst

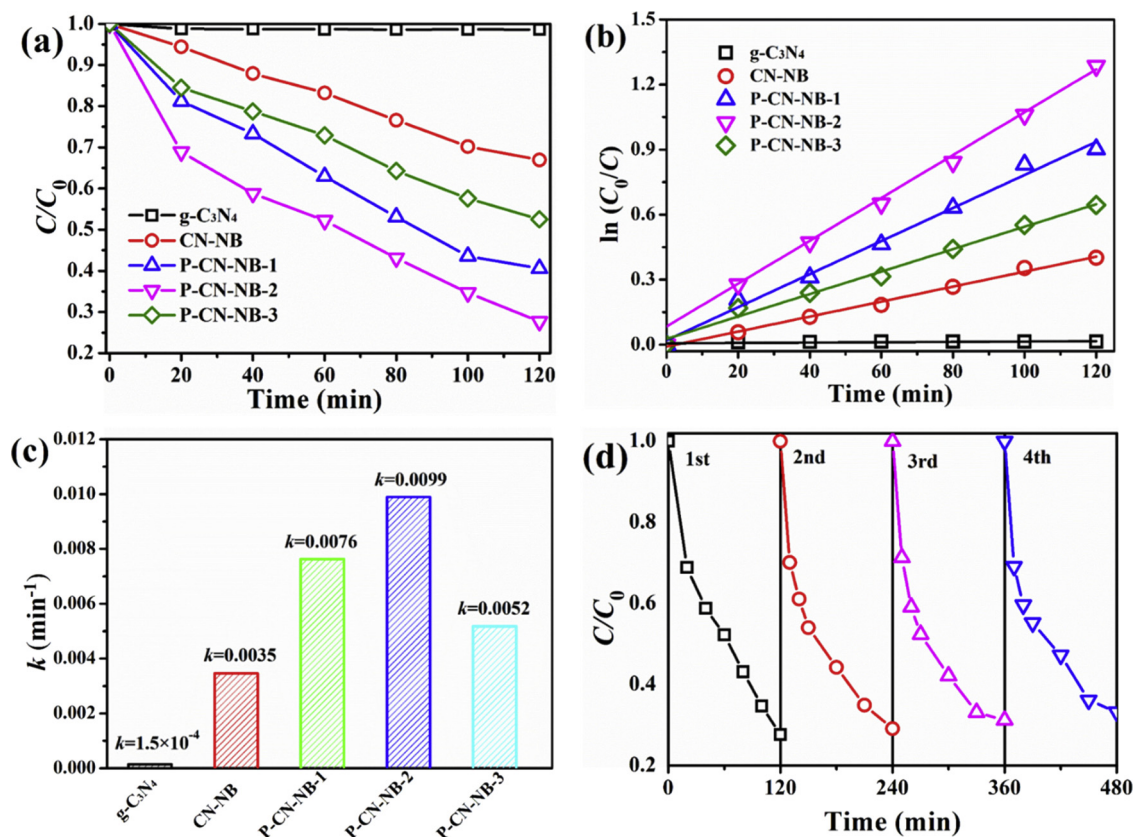


Fig. 7. (a) Photocatalytic degradation of HBA, (b) the first-order-kinetic plots of the $g\text{-C}_3\text{N}_4$, and CN-NB, (c) the kinetic values of the P-CN-NB for the degradation of HBA, and (d) the stability of the P-CN-NB-2 for the degradation of HBA.

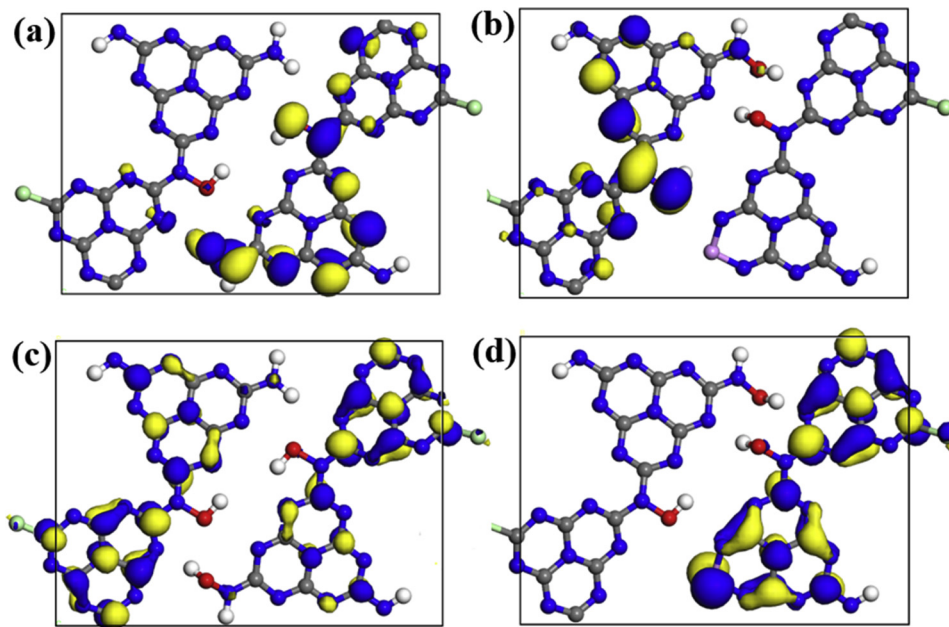


Fig. 8. HOMO orbital of (a) CN-NB and (b) P-CN-NB, and LUMO orbital of (c) CN-NB, and (d) P-CN-NB, respectively.

remains nearly the same, indicating that P-CN-NB-2 is a stable catalyst and can be used repeatedly for the wastewater treatment. To illustrate the anti-oxidation ability of N-P bonding, we carried out the XPS analysis of the used P-CN-NB-2 (Fig. S8). For the P2p of the used P-CN-NB-2, only minor change in P–N bond was found, indicating the stability of P–N bond. The results were also in accordance with that of recycling tests.

The experimentally observed enhancement in the apparent rate

constant in CN-NB and P-CN-NB may be explained by the difference in the HOMO and LUMO configurations. Within the plain $g\text{-C}_3\text{N}_4$ (Fig. S9), the orbitals of both HOMO and LUMO distributed reasonably homogenously, with a large separation between the orbitals of different atoms. In contrast, the HOMO orbitals in both CN-NB and P-CN-NB are highly asymmetric (Fig. 8a and b), with that of the former concentrated on the right-hand side, and that of the latter on the left-hand side. Once the electrons are elevated into LUMO orbitals, significant

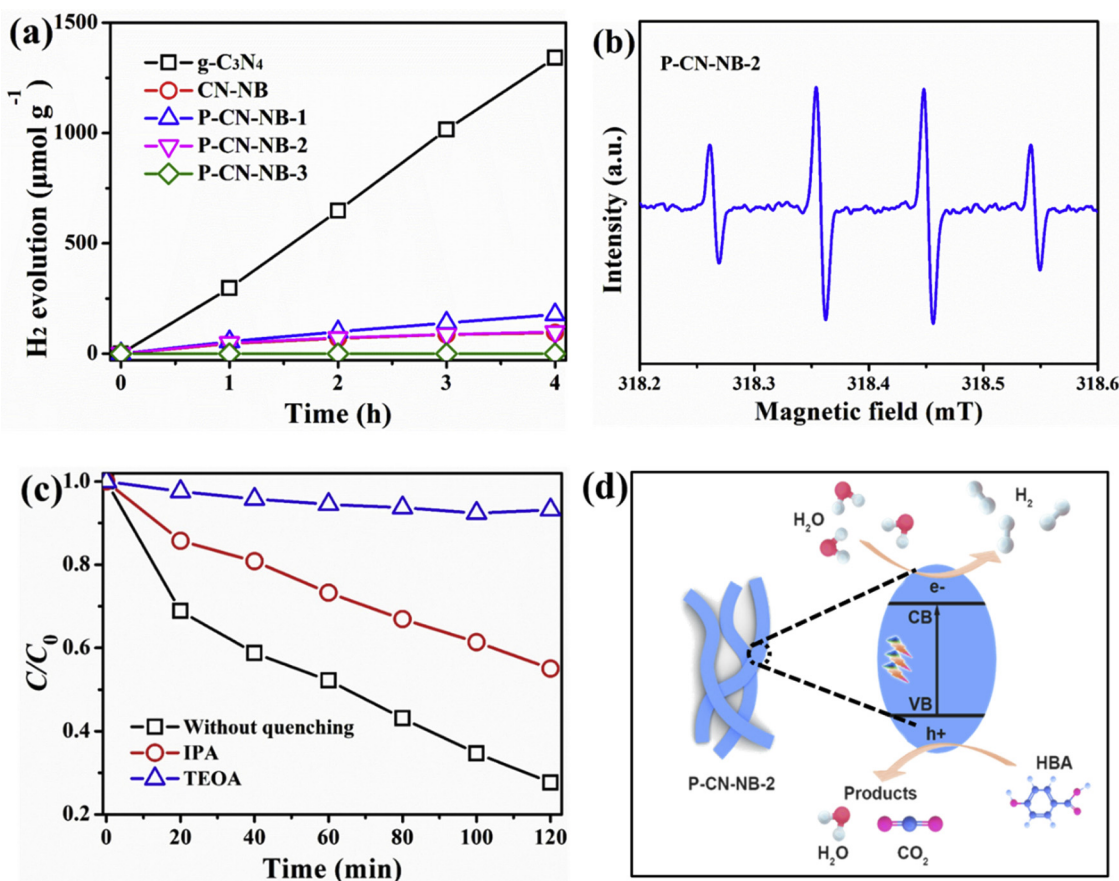


Fig. 9. (a) H₂ evolution efficiency of the prepared samples, (b) ESR spectra in the presence of HBA, (c) photocatalytic degradation of HBA of the P-CN-NB in the presence of TEOA and TBA, and (d) schematic illustration of the proposed mechanism for the P-CN-NB-2 system.

changes are observed. For CN-NB, orbitals become more evenly distributed with an improved separation (Fig. 8c). More interestingly, within P-CN-NB orbitals are shifted into the left-hand side, and the separations between orbitals of different atoms are significantly reduced (Fig. 8d). The charge carriers (electron-hole pairs) are distributed more uniformly and intimately on the right-hand side channel, which is beneficial for the charge carrier transport and electron-hole separation. Hence the DFT results are consistent with our experimental ones in that, both CN-NB and P-CN-NB have better catalysis efficiency, and the enhancement in the latter is much more significant.

Furthermore, the hydrogen evolution efficiency of the prepared samples was evaluated under the visible light irradiations (Fig. 9a). On g-C₃N₄, about 297 μmol g⁻¹ h⁻¹ H₂ can be produced. However, the H₂ production amount of CN-NB and P-CN-NB was lower than that of g-C₃N₄. This phenomenon can be attributed to the deeper CB edge of CN-NB and P-CN-NB. Therefore, the reduction ability of CN-NB and P-CN-NB is weaker. It should be noted that the H₂ evolution efficiency of P-CN-NB-1 was about 1.8 times of CN-NB and P-CN-NB-2, suggesting that proper P dopant can enhance the photocatalytic H₂ production. In general, adequate P doping can improve both the oxidation and reduction efficiency.

To shed light onto the photocatalytic mechanism of the P-CN-NB-2, electron spin resonance (ESR) and trapping experiments were carried out. During the ESR process, we simulated the same reaction condition except for the addition of 5,5-Dimethyl-1-pyrroline N-oxide (DMPO) as a trapping agent. As shown in Fig. 9b, after the visible light irradiations for 10 min, four peaks with the intensity ratio of 1:2:2:1 were found, suggesting the typical signal of ·OH. This phenomenon indicates that ·OH may be the active species in the photocatalytic degradation of HBA. In addition, we carried out the quenching experiments to further

detect the active species (Fig. 9c). During the process, IPA (0.02 M) or TEOA (0.01 M) were selected as an ·OH scavenger or an h⁺ scavenger, respectively. When the IPA was added into the solution, the photocatalytic activity of P-CN-NB-2 decreased slightly from 77.3% to 45%. However, after the addition of TEOA (0.01 M), the HBA degradation efficiency reached nearly zero. The above results indicated that both ·OH and h⁺ participated in the degradation, and h⁺ played a crucial role in the process of degradation of HBA.

On the basis of the above ESR analysis, trapping experiments results, and the band structure (Fig. 4d) of P-CN-NB-2, a tentative mechanism of the P-CN-NB-2 for HBA degradation was proposed (Fig. 9d). With the irradiations of the visible light ($\lambda > 420$ nm), the electrons and holes were produced, during which electrons were motivated to the CB, and creating holes on the VB. The position of reducing O₂ to ·O₂⁻ was located at about -0.33 eV, which is more negative than the CB of P-CN-NB-2 (-0.04 eV). Therefore, ·O₂⁻ may not be produced in this system. Besides, only a slight amount of H₂ can be detected, which can also be ascribed to the position of the CB band. Simultaneously, holes as a strong oxidant can directly degrade pollutants. Meanwhile, holes can also be transformed to ·OH since the VB position of P-CN-NB-2 (2.15 eV) was more positive than that of h⁺ / -OH (1.99 eV).

4. Conclusions

In summary, we synthesized P doped carbon nitride with a nanoblet structure via a one-step solvothermal approach. The doped photocatalyst exhibited about 66 times enhanced apparent rate constant on HBA degradation than bulk g-C₃N₄, much higher than most reported g-C₃N₄-based photocatalysts. Such an increased activity can be attributed to the introduction of P, which helps to extend the absorption

threshold, to enhance the conductivity, to tune the electronic band structures, to tailor the morphologies, and to facilitate the separation of electron-hole pairs. The DFT results for HOMO and LUMO indicated that the configurations within P—CN—NB are more favorable for the charge carrier transport and electron-hole separation, hence they support the observed enhancement in the catalyst efficiency of P—CN—NB. Calculation results also suggested that the narrowing of the band-gap on P—CN—NB was mainly driven by the contribution from the 2p bands in C, N, and 3p band in P dopants. This work provides a new concept for the synthesis of P doped carbon nitride nanobelt via a solvothermal method. It is expected that similar approaches can be developed to prepare heteroatom doped catalysts with various novel compositions, which will significantly enhance photocatalytic capabilities for environmentally friendly applications.

Conflict of Interest

Nothing declared.

Acknowledgments

This work was partially supported by the National Science and Technology Major Project (NO. 2016ZX05040003), the Fundamental Research Funds for the Central Universities (NO. 17CX06027), ARC Discovery Projects (DP150103026 and DP170104264) and the CSC scholarship (201806450064).

Appendix A. Supplementary data

Supplementary material related to this article can be found, in the online version, at doi:<https://doi.org/10.1016/j.apcatb.2019.117931>.

References

- [1] L. Shi, Y. Yin, L.-C. Zhang, S. Wang, M. Sillanpää, H. Sun, Design and engineering heterojunctions for the photoelectrochemical monitoring of environmental pollutants: a review, *Appl. Catal. B-Environ.* 248 (2019) 405–422.
- [2] W. Tian, H. Zhang, Z. Qian, T. Ouyang, H. Sun, J. Qin, M.O. Tadé, S. Wang, Bread-making synthesis of hierarchically Co@C nanoarchitecture in heteroatom doped porous carbons for oxidative degradation of emerging contaminants, *Appl. Catal. B-Environ.* 225 (2018) 76–83.
- [3] H. Bian, Y. Ji, J. Yan, P. Li, L. Li, Y. Li, S. Frank Liu, In situ synthesis of few-layered g-C₃N₄ with vertically aligned MoS₂ loading for boosting solar-to-hydrogen generation, *Small* 14 (2017) 1703003.
- [4] W.J. Ong, L.L. Tan, Y.H. Ng, S.T. Yong, S.P. Chai, Graphitic carbon nitride (g-C₃N₄)-based photocatalysts for artificial photosynthesis and environmental remediation: are we a step closer to achieving sustainability? *Chem. Rev.* 116 (2016) 7159–7329.
- [5] T. Di, B. Zhu, B. Cheng, J. Yu, J. Xu, A direct Z-scheme g-C₃N₄/SnS₂ photocatalyst with superior visible-light CO₂ reduction performance, *J. Catal.* 352 (2017) 532–541.
- [6] S.J. Bonyhady, N. Holzmann, G. Frenking, A. Stasch, C. Jones, Synthesis, characterization, and computational analysis of the dianilate dianion, [H₃Al-AlH₃]⁽²⁻⁾: a valence isoelectronic analogue of ethane, *Angew. Chem. Int. Ed.* 56 (2017) 8527–8531.
- [7] H. Sun, Y. Bai, Y. Cheng, W. Jin, N. Xu, Preparation and characterization of visible-light-driven carbon–sulfur-codoped TiO₂ photocatalysts, *Ind. Eng. Chem. Res.* 45 (2006) 4971–4976.
- [8] B. Sun, Y. Chen, L. Tao, H. Zhao, G. Zhou, Y. Xia, H. Wang, Y. Zhao, Nanorods array of SnO₂ quantum dots interspersed multiphase TiO₂ heterojunctions with highly photocatalytic water splitting and self-rechargeable battery-like applications, *ACS Appl. Mater. Interfaces* 11 (2018) 2071–2081.
- [9] J. Gao, B. Jiang, C. Ni, Y. Qi, Y. Zhang, N. Oturan, M.A. Oturan, Non-precious Co₃O₄–TiO₂/Ti cathode based electrocatalytic nitrate reduction: preparation, performance and mechanism, *Appl. Catal. B-Environ.* 254 (2019) 391–402.
- [10] Y. Wang, R. Shi, J. Lin, Y. Zhu, Enhancement of photocurrent and photocatalytic activity of ZnO hybridized with graphite-like C₃N₄, *Energy Environ. Sci.* 4 (2011) 2922.
- [11] H. Zhang, W. Tian, Y. Li, H. Sun, M.O. Tadé, S. Wang, A comparative study of metal (Ni, Co, or Mn)-borate catalysts and their photodeposition on rGO/ZnO nanoarrays for photoelectrochemical water splitting, *J. Mater. Chem. A* 6 (2018) 24149–24156.
- [12] Y. Lan, Z. Liu, Z. Guo, X. Li, L. Zhao, L. Zhan, M. Zhang, A ZnO/ZnFe₂O₄ uniform core-shell heterojunction with a tubular structure modified by NiOOH for efficient photoelectrochemical water splitting, *Dalton Trans.* 47 (2018) 12181–12187.
- [13] H. Zhang, W. Tian, Y. Li, H. Sun, M.O. Tadé, S. Wang, Heterostructured WO₃@CoWO₄ bilayer nanosheets for enhanced visible-light photo, electro and photoelectro-chemical oxidation of water, *J. Mater. Chem. A* 6 (2018) 6265–6272.
- [14] H. Li, H. Yu, X. Quan, S. Chen, Y. Zhang, Uncovering the key role of the fermi level of the electron mediator in a Z-scheme photocatalyst by detecting the charge transfer process of WO₃-metal-gC₃N₄ (Metal = Cu, Ag, Au), *ACS Appl. Mater. Interfaces* 8 (2016) 2111–2119.
- [15] D. Chen, Z. Liu, Dual-axial gradient doping (Zr and Sn) on hematite for promoting charge separation in photoelectrochemical water splitting, *ChemSusChem* 11 (2018) 3438–3448.
- [16] D. Chen, Z. Liu, Z. Guo, W. Yan, Y. Xin, Enhancing light harvesting and charge separation of Cu₂O photocathodes with spatially separated noble-metal cocatalysts towards highly efficient water splitting, *J. Mater. Chem. A* 6 (2018) 20393–20401.
- [17] J. Tian, Z. Zhao, A. Kumar, R.I. Boughton, H. Liu, Recent progress in design, synthesis, and applications of one-dimensional TiO₂ nanostructured surface heterostructures: a review, *Chem. Soc. Rev.* 43 (2014) 6920–6937.
- [18] S.J.A. Moniz, S.A. Shevlin, D.J. Martin, Z.-X. Guo, J. Tang, Visible-light driven heterojunction photocatalysts for water splitting – a critical review, *Energy Environ. Sci.* 8 (2015) 731–759.
- [19] L. Shi, L. Yang, W. Zhou, Y. Liu, L. Yin, X. Hai, H. Song, J. Ye, Photoassisted construction of holey defective g-C₃N₄ photocatalysts for efficient visible-light-driven H₂O₂ production, *Small* 14 (2018) 1703142.
- [20] L. Chen, J. Song, Tailored graphitic carbon nitride nanostructures: synthesis, modification, and sensing applications, *Adv. Funct. Mater.* 27 (2017) 1702695.
- [21] L. Zhang, F. Mao, L.R. Zheng, H.F. Wang, X.H. Yang, H.G. Yang, Tuning metal catalyst with metal–C₃N₄ interaction for efficient CO₂ electroreduction, *ACS Catal.* 8 (2018) 11035–11041.
- [22] Z.W. Tong, D. Yang, Y.Y. Sun, Y.H. Nan, Z.Y. Jiang, Tubular g-C₃N₄ isotype heterojunction: enhanced visible-light photocatalytic activity through cooperative manipulation of oriented electron and hole transfer, *Small* 12 (2016) 4093–4101.
- [23] G.H. Moon, M. Fujitsuka, S. Kim, T. Majima, X. Wang, W. Choi, Eco-friendly photochemical production of H₂O₂ through O₂ reduction over carbon nitride frameworks incorporated with multiple heteroelements, *ACS Catal.* 7 (2017) 2886–2895.
- [24] G. Liu, G. Zhao, W. Zhou, Y. Liu, H. Pang, H. Zhang, D. Hao, X. Meng, P. Li, T. Kako, J. Ye, In situ bond modulation of graphitic carbon nitride to construct p-n homojunctions for enhanced photocatalytic hydrogen production, *Adv. Funct. Mater.* 26 (2016) 6822–6829.
- [25] W. Jiang, W. Luo, R. Zong, W. Yao, Z. Li, Y. Zhu, Polyaniiline/carbon nitride nanosheets composite hydrogel: a separation-free and high-efficient photocatalyst with 3D hierarchical structure, *Small* 12 (2016) 4370–4378.
- [26] M.Y. Ye, Z.H. Zhao, Z.F. Hu, L.Q. Liu, H.M. Ji, Z.R. Shen, T.Y. Ma, 0D/2D heterojunctions of vanadate quantum dots/graphitic carbon nitride nanosheets for enhanced visible-light-driven photocatalysis, *Angew. Chem. Int. Ed.* 56 (2017) 8407–8411.
- [27] J. Fu, B. Zhu, C. Jiang, B. Cheng, W. You, J. Yu, Hierarchical porous O-doped g-C₃N₄ with enhanced photocatalytic CO₂ reduction activity, *Small* 13 (2017) 1603938.
- [28] R. Hao, G. Wang, H. Tang, L. Sun, C. Xu, D. Han, Template-free preparation of macro/mesoporous g-C₃N₄/TiO₂ heterojunction photocatalysts with enhanced visible light photocatalytic activity, *Appl. Catal., B-Environ.* 187 (2016) 47–58.
- [29] Q. Hao, X. Niu, C. Nie, S. Hao, W. Zou, J. Ge, D. Chen, W. Yao, A highly efficient g-C₃N₄/SiO₂ heterojunction: the role of SiO₂ in the enhancement of visible light photocatalytic activity, *Phys. Chem. Chem. Phys.* 18 (2016) 31410–31418.
- [30] D. Zheng, X. Cao, X. Wang, Precise formation of a hollow carbon nitride structure with a Janus surface to promote water splitting by photoredox catalysis, *Angew. Chem. Int. Ed.* 55 (2016) 11512–11516.
- [31] W. Wu, J. Zhang, W. Fan, Z. Li, L. Wang, X. Li, Y. Wang, R. Wang, J. Zheng, M. Wu, H. Zeng, Remediating defects in carbon nitride to improve both photooxidation and H₂ generation efficiencies, *ACS Catal.* 6 (2016) 3365–3371.
- [32] Q. Yan, C. Zhao, L. Zhang, Y. Hou, S. Wang, P. Dong, F. Lin, Y. Wang, Facile two-step synthesis of porous carbon nitride with enhanced photocatalytic activity using a soft template, *ACS Sustain. Chem. Eng.* 7 (2019) 3866–3874.
- [33] Y. Jun, E.Z. Lee, X. Wang, W.H. Hong, G.D. Stucky, A. Thomas, From melamine-cyanuric acid supramolecular aggregates to carbon nitride hollow spheres, *Adv. Funct. Mater.* 23 (2013) 3661–3667.
- [34] X. She, J. Wu, H. Xu, J. Zhong, Y. Wang, Y. Song, K. Nie, Y. Liu, Y. Yang, M.-T.F. Rodrigues, R. Vajtai, J. Lou, D. Du, H. Li, P.M. Ajayan, High efficiency photocatalytic water splitting using 2D α -Fe₂O₃/g-C₃N₄ Z-Scheme catalysts, *Adv. Energy Mater.* 7 (2017) 1700025.
- [35] Q. Gu, Y. Liao, L. Yin, J. Long, X. Wang, C. Xue, Template-free synthesis of porous graphitic carbon nitride microspheres for enhanced photocatalytic hydrogen generation with high stability, *Appl. Catal. B-Environ.* 165 (2015) 503–510.
- [36] Q. Gu, H. Sun, Z. Xie, Z. Gao, C. Xue, MoS₂-coated microspheres of self-sensitized carbon nitride for efficient photocatalytic hydrogen generation under visible light irradiation, *Appl. Surf. Sci.* 396 (2017) 1808–1815.
- [37] Y. Wang, H. Wang, F. Chen, F. Cao, X. Zhao, S. Meng, Y. Cui, Facile synthesis of oxygen doped carbon nitride hollow microsphere for photocatalysis, *Appl. Catal. B-Environ.* 206 (2017) 417–425.
- [38] S. Wang, F. He, P. Dong, Z. Tai, C. Zhao, Y. Wang, F. Liu, L. Li, Simultaneous morphology, band structure, and defect optimization of graphitic carbon nitride microspheres by the precursor concentration to boost photocatalytic activity, *J. Mater. Res.* 33 (2018) 3917–3927.
- [39] Y. Cui, Z. Ding, X. Fu, X. Wang, Construction of conjugated carbon nitride nanoarchitectures in solution at low temperatures for photoredox catalysis, *Angew. Chem. Int. Ed.* 51 (2012) 11814–11818.
- [40] B. Jing, Z. Ao, Z. Teng, C. Wang, J. Yi, T. An, Density functional theory study on the effects of oxygen groups on band gap tuning of graphitic carbon nitrides for possible photocatalytic applications, *Sustain. Mater. Technol.* 16 (2018) 12–22.

[41] M. Seredych, T.J. Bandosz, Nitrogen enrichment of S-doped nanoporous carbon by g-C₃N₄: insight into photosensitivity enhancement, *Carbon* 107 (2016) 895–906.

[42] H. Wang, B. Wang, Y. Bian, L. Dai, Enhancing photocatalytic activity of graphitic carbon nitride by codoping with P and C for efficient hydrogen generation, *ACS Appl. Mater. Interfaces* 9 (2017) 21730–21737.

[43] Z. Lan, G. Zhang, X. Wang, A facile synthesis of Br-modified g-C₃N₄ semiconductors for photoredox water splitting, *Appl. Catal. B-Environ.* 192 (2016) 116–125.

[44] Z. Hu, L. Yuan, Z. Liu, Z. Shen, J.C. Yu, An elemental phosphorus photocatalyst with a record high hydrogen evolution efficiency, *Angew. Chem. Int. Ed.* 55 (2016) 9580–9585.

[45] J. Ran, T.Y. Ma, G. Gao, X.-W. Du, S.Z. Qiao, Porous P-doped graphitic carbon nitride nanosheets for synergistically enhanced visible-light photocatalytic H₂ production, *Energy Environ. Sci.* 8 (2015) 3708–3717.

[46] S. Guo, Z. Deng, M. Li, B. Jiang, C. Tian, Q. Pan, H. Fu, Phosphorus-doped carbon nitride tubes with a layered micro-nanostructure for enhanced visible-light photocatalytic hydrogen evolution, *Angew. Chem. Int. Ed.* 55 (2016) 1830–1834.

[47] X. Wang, K. Maeda, X. Chen, K. Takanabe, K. Domen, Y. Hou, X. Fu, M. Antonietti, Polymer semiconductors for artificial photosynthesis: hydrogen evolution by mesoporous graphitic carbon nitride with visible light, *J. Am. Chem. Soc.* 131 (2009) 1680–1681.

[48] S.J. Clark, M.D. Segall, C.J. Pickard, P.J. Hasnip, M.I. Probert, K. Refson, M.C. Payne, First principles methods using CASTEP, *Zeits. für Kris.-Crystal. Mater.* 220 (2005) 567–570.

[49] J.P. Perdew, K. Burke, M. Ernzerhof, Generalized gradient approximation made simple, *Phys. Rev. Lett.* 77 (1996) 3865.

[50] H. Yu, R. Shi, Y. Zhao, T. Bian, Y. Zhao, C. Zhou, G.I. Waterhouse, L.Z. Wu, C.H. Tung, T. Zhang, Alkali-assisted synthesis of nitrogen deficient graphitic carbon nitride with tunable band structures for efficient visible-light-driven hydrogen evolution, *Adv. Mater.* 29 (2017) 1605148.

[51] Y. Zheng, L. Lin, B. Wang, X. Wang, Graphitic carbon nitride polymers toward sustainable photoredox catalysis, *Angew. Chem. Int. Ed.* 54 (2015) 12868–12884.

[52] P. Niu, L.C. Yin, Y.Q. Yang, G. Liu, H.M. Cheng, Increasing the visible light absorption of graphitic carbon nitride (melon) photocatalysts by homogeneous self-modification with nitrogen vacancies, *Adv. Mater.* 26 (2014) 8046–8052.

[53] B.V. Lotsch, M. Döblinger, J. Sehnert, L. Seyfarth, J. Senker, O. Oeckler, W. Schnick, Unmasking melon by a complementary approach employing electron diffraction, solid-state NMR spectroscopy, and theoretical calculations—structural characterization of a carbon nitride polymer, *Chem. Eur. J.* 13 (2007) 4969–4980.

[54] Q. Gu, Z. Gao, C. Xue, Self-sensitized carbon nitride microspheres for long-lasting visible-light-driven hydrogen generation, *Small* 12 (2016) 3543–3549.

[55] S. Wang, Q. Yan, P. Dong, C. Zhao, Y. Wang, F. Liu, L. Li, Morphology and band structure regulation of graphitic carbon nitride microspheres by solvothermal temperature to boost photocatalytic activity, *Appl. Phys. A* 124 (2018) 416.

[56] Z. Mo, X. She, Y. Li, L. Liu, L. Huang, Z. Chen, Q. Zhang, H. Xu, H. Li, Synthesis of g-C₃N₄ at different temperatures for superior visible/UV photocatalytic performance and photoelectrochemical sensing of MB solution, *RSC Adv.* 5 (2015) 101552–101562.

[57] V.W. Lau, M.B. Mesch, V. Doppel, V. Blum, J. Senker, B.V. Lotsch, Low-molecular-weight carbon nitrides for solar hydrogen evolution, *J. Am. Chem. Soc.* 137 (2015) 1064–1072.

[58] X. Shi, M. Fujitsuka, S. Kim, T. Majima, Faster electron injection and more active sites for efficient photocatalytic H₂ evolution in g-C₃N₄/MoS₂ hybrid, *Small* 14 (2018) 1703277.

[59] M. Zhu, S. Kim, L. Mao, M. Fujitsuka, J. Zhang, X. Wang, T. Majima, Metal-free photocatalyst for H₂ evolution in visible to near-infrared region: black phosphorus/graphitic carbon nitride, *J. Am. Chem. Soc.* 139 (2017) 13234–13242.

[60] C. Zhao, S. Wang, Q. Yan, P. Dong, Y. Wang, F. Liu, L. Li, Nitrogen defects-rich 0D/2D α -Fe₂O₃/g-C₃N₄ Z-scheme photocatalyst for enhanced photooxidation and H₂ evolution efficiencies, *Nano* 13 (2018) 1850086.

[61] Y. Liu, H. Zhang, J. Ke, J. Zhang, W. Tian, X. Xu, X. Duan, H. Sun, M.O. Tade, S. Wang, 0D (MoS₂)/2D (g-C₃N₄) heterojunctions in Z-scheme for enhanced photocatalytic and electrochemical hydrogen evolution, *Appl. Catal. B-Environ.* 228 (2018) 64–74.

[62] X. Li, D. Xie, H. Park, M. Zhu, T.H. Zeng, K. Wang, J. Wei, D. Wu, J. Kong, H. Zhu, Ion doping of graphene for high-efficiency heterojunction solar cells, *Nanoscale* 5 (2013) 1945–1948.

[63] Y. Zhang, M. Antonietti, Phosphorus-doped carbon nitride solid: enhanced electrical conductivity and photocurrent generation, *J. Am. Chem. Soc.* 5 (2010) 1307–1311.

[64] X. Wang, K. Maeda, A. Thomas, K. Takanabe, G. Xin, J.M. Carlsson, K. Domen, M. Antonietti, A metal-free polymeric photocatalyst for hydrogen production from water under visible light, *Nat. Mater.* 8 (2009) 76.

[65] G. Dong, K. Zhao, L. Zhang, Carbon self-doping induced high electronic conductivity and photoreactivity of g-C₃N₄, *Chem. Commun.* 48 (2012) 6178–6180.